Protonation of Al-grafted mesostructured silica nanoparticles (MSN): Acidity and catalytic activity for cumene conversion

M.R. Sazegar [a], A.A. Jalil [b], S. Triwahyono [a,c,*], R.R. Mukti [d], M. Aziz [a], M.A.A. Aziz [b], H.D. Setiabudi [e], N.H.N. Kamarudin [b]

[a] Department of Chemistry, Faculty of Science, Universiti Teknologi Malaysia, 81310 UTM Johor Bahru, Johor, Malaysia
[b] Institute Hydrogen Economy, Department of Chemical Eng., Faculty of Chemical Eng., Universiti Teknologi Malaysia, 81310 UTM Johor Bahru, Johor, Malaysia
[c] Ibnu Sina Institute for Fundamental Science Studies, Universiti Teknologi Malaysia, 81310 UTM Johor Bahru, Johor, Malaysia
[d] Division of Inorganic and Physical Chemistry, Fac. of Mathematics and Natural Sciences, Institut Teknologi Bandung, Jl Ganesha No 10, Bandung 40132, Indonesia
[e] Faculty of Chemical and Natural Resources Engineering, Universiti Malaysia Pahang, 26300 Gambang, Kuantan, Pahang, Malaysia

HIGHLIGHTS

- Protonation of Al-grafted MSN formed strong Brønsted and Lewis acidic sites.
- Cumene conversion over HAlMSN proceeded via cracking and dehydrogenation routes.
- Cracking proceeded over protonic acid sites forming propylene, benzene and toluene.
- Dehydrogenation proceeded over Lewis acidic sites forming α-methylstyrene.
- The high activity of HAlMSN in cumene conversion was observed for more than 60 h.

GRAPHICAL ABSTRACT
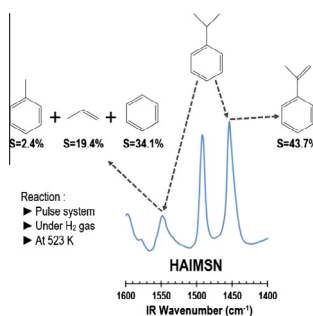
ABSTRACT

The hexagonal structure of the mesostructured silica nanoparticles (MSN) based solid acid catalyst was synthesized using 1,2-propanediol as a co-solvent by sol–gel method, followed by aluminum grafting and protonation. The activity of the catalysts was tested for cumene conversion in a pulse microcatalytic reactor at 323–573 K. XRD, TEM and N_2 physisorption results confirmed the hexagonal ordered structure with a pore diameter of 3.4–4.0 nm, a particle size of 70–120 nm and a surface area of 588–995 m^2/g. Solid state NMR and IR results confirmed that the aluminum grafting and protonation form framework and extra-framework aluminums which led to generating strong Brønsted and Lewis acidic sites. High activity in the cumene conversion was only observed on HAlMSN producing propylene, benzene, toluene via a cracking on protonic acid sites and producing a main product of α-methylstyrene via a dehydrogenation on Lewis acidic sites at high reaction temperature. While only α-methylstyrene and higher hydrocarbon ($\geqslant C_{10}$) were produced at low reaction temperature showing the permanent Brønsted acid sites did not involve in the cumene conversion. It is suggested that the presence of hydrogen and strong Lewis acid sites increased the stability and activity of the HAlMSN catalyst in the cumene conversion. Although the small deactivation of HAlMSN was observed during the reaction due to the formation of small coke deposits on the surface, the reactivation recovered the activity of catalyst and the high activity was still observed after 60 h of reaction. The high stability and activity of HAlMSN in the cumene conversion can be considered as a method for the production of α-methylstyrene via a dehydrogenation process.

© 2013 Elsevier B.V. All rights reserved.

* Corresponding author at: Ibnu Sina Institute for Fundamental Science Studies, Universiti Teknologi Malaysia, 81310 UTM Johor Bahru, Johor, Malaysia. Tel.: +60 7 5536076; fax: +60 7 5536080.
 E-mail address: sugeng@utm.my (S. Triwahyono).

1. Introduction

Mesoporous silica material with a large surface area and pore size diameter has high potential for applications in chemical processes as a catalyst [1–5]. This material exhibits three-dimensional and two-dimensional structures within an amorphous pore wall but the structure suffers weak stability and activity in the catalysis. MCM-41, MCM-48 and SBA-15 are typical mesoporous silica materials with a large surface area and pore diameter. Recently, extensive research on the development of new mesoporous material has been undertaken [6–8]. Okubo et al. [9] and Inagaki et al. [10] have explored the development of nano-sized mesostructured silica material. They have succeeded in preparing mesostructured silica nanoparticles (MSN) with an average particle and pore size of 70–100 and 2.54 nm, respectively. Upon its development, MSN was widely applied in drug delivery systems, cancer therapy [11], inflammatory cardiovascular treatment [12] and had been used as an excellent adsorbent in the environmental protection process [13–15].

For application in gas reaction, numerous efforts have been made to improve the hydrothermal stability and enhance the acidity and activity of mesoporous materials as solid acid catalysts [16–20]. The modification of mesoporous materials by Al, Ga, Ir, W, Mo, Rh and Zr enabled improvements in the concentration of active sites, activity and stability of the mesoporous silica materials [21–25]. The introduction of mixed metal oxides on the mesoporous material was also found to improve the activity of the catalyst. Li et al. reported that the introduction of WO_3/ZrO_2 on the mesoporous channels of SBA-15 increased the acidity and activity of the catalyst, though the presence of WO_3/ZrO_2 decreased the surface area and pore volume of SBA-15 [26]. In particular, the addition of 1 wt% Pt activated the catalyst in *n*-pentane isomerization with selectivity toward isopentane reaching about 97%. Wang et al. studied the activity of sulfated zirconia (SZ) supported on MCM-41 in *n*-butane isomerization [27]. They concluded that the activity and stability of the catalyst strongly depended on the number of the sulfur loading, the balanced distribution of the Lewis–Brønsted acid sites and high dispersion of zirconia [27,28].

In contrast, Al loaded on MCM-41 was found to possess a high concentration of both Lewis and Brønsted acidic sites which led to an increase in the activity in cracking and/or the isomerization process [29,30]. Accordingly, Jana et al. [31] reported the synthesis of Al-MCM-41 with various Si/Al ratios with four different synthesis methods: sol–gel, hydrothermal, template cation exchange and grafting. The results showed that the acidity and catalytic activity in cumene cracking were enhanced with the increasing amount of Al content in the framework of the catalysts. The sol–gel and hydrothermal methods exhibited the highest and lowest activity in cumene cracking, which may be coincidentally due to the highest and lowest acidity of the Al-MCM-41. The Al-MCM-41 showed the highest activity in cumene cracking as compared to SBA-15, HY and ZSM-5 due to its high acidity [32]. In another report, Kao et al. synthesized well-ordered mesoporous MCM-48 via the assembly of dried BEA and ZSM-5 precursors with gemini surfactant [33]. The cubic structure of the products exhibited hydrothermal stability under steam, treated at 800 °C for 12 h. The MCM-48 prepared by the ZSM-5 precursor showed higher catalytic activity in cumene cracking than that prepared by the BEA precursor. The ordered hexagonal mesopores of the MCM-41 type are usually prepared via an alkaline media, while the mesoporous SBA-15 is synthesized directly using a tri-block polymer of P123 in aqueous acidic solution. Kumaran et al. studied the effect of various ratios of Si/Al with the range 11.4–78.4 in the acidity and activity of Al-SBA-15 for cumene conversion [34]. They found that the hexagonal mesostructure of Al-SBA-15 was retained after Al loading and the surface area was increased with the increasing Al content [35,36]. In contrast, Kao et al. reported that post-synthesis Al loading on SBA-15 reduces the surface area due to the collapse of the pore structure by the alkaline media [37]. On the other hand, Yue et al. prepared the Al loaded on SBA-15 with an Si/Al ratio of 10 and 20 by the direct aluminum incorporation method [36]. The application to cumene cracking showed that the catalytic activity increased with the Si/Al ratio, indicating the strong acidic sites' dependence on the reaction.

Along this line, our research group also focused on the development of mesostructured silica nanoparticles (MSN) for acid catalytic reaction due to the excellent properties of large surface area, bigger pore size diameter and, particularly the nano-size particle which offers better properties and activities compared to conventional mesoporous materials. In this report, we have prepared MSN by sol–gel method which resulted MSN with a particle size of 70–120 nm and pore diameter of 3.37–4.00 nm, respectively. The introduction of aluminum, inside and outside the pores, followed by protonation was found to enhance the activity and stability of MSN. The MSN, AlMSN and protonated AlMSN (HAlMSN) have been tested in the cumene catalytic conversion in the presence and absence of molecular hydrogen. The result showed that only HAlMSN was active in cumene conversion. Neither MSN nor aluminum-grafted MSN (AlMSN) exhibited activity in the cumene conversion regardless of the carrier gas. A comparison of the activity and acidic properties of MSN type catalysts, mesporous materials and silica based catalysts is discussed. The roles of protonic and Lewis acidic sites in the producing of α-methylstyrene, propylene, benzene and toluene from cumene are also discussed.

2. Experimental

2.1. Catalyst synthesis

The synthesis of pure-silica MSN support followed the procedure of the previous report [14]. The as-synthesized MSN was prepared as described below. Cetyltrimethylammonium bromide (CTAB, 1.17 g) was dissolved in a solution containing double distilled water (180 g) and 1,2-propanediol (30 ml) in an aqueous ammonia solution (7.2 ml, 25%). After vigorous stirring for approximately 30 min at 323 K, tetraethylorthosilicate (TEOS, 1.43 ml) and 3-aminopropyl triethoxysilane (APTES, 0.263 ml) were added to the mixture. The resulting mixture was stirred for an additional 2 h at 323 K and allowed to rest for 20 h at the same temperature. The sample was collected by centrifugation at 20,000 rpm for 30 min and washed with deionized water and absolute ethanol 3 times. The surfactant was removed by heating MSN (1 g) in an NH_4NO_3 (0.3 g) and ethanol (40 ml) solution at 333 K. The surfactant-free product was collected by centrifugation and dried at 383 K overnight prior to calcination in air at 823 K for 3 h. The acidic sites of the sample were prepared by aluminum-grafting on the template-free MSN at 353 K for 10 h followed by centrifugation and dried at 383 K overnight prior to calcination in air at 823 K for 3 h. Sodium aluminate (Sigma–Aldrich) was used as a precursor of aluminum. The aluminum-grafted MSN was denoted as AlMSN. Whereas, the protonated AlMSN (HAlMSN) was prepared by protonation of AlMSN (1 g) using aqueous solution of NH_4NO_3 (2.5 g in 50 ml of double distilled water) at 333 K for 16 h followed by removal of solution, drying at 383 K overnight and calcination at 823 K for 3 h in air.

The mixed γ-Al_2O_3–SiO_2 were prepared by physical and thermal mixing methods. For the physical mixing method, commercial γ-Al_2O_3 (Merck) was physically mixed with amorphous SiO_2 (Merck) support at room temperature without any solution. While,

for the thermal mixing method, the catalyst was prepared by treatment of amorphous SiO_2 support with γ-Al_2O_3 in a 5% NaOH solution at 353 K, followed by drying at 383 K overnight and calcination at 823 K for 3 h in air. The Si/Al ratio of both mixed γ-Al_2O_3–SiO_2 catalysts was adjusted to 20. The N_2 physisorption showed the specific surface area of simple and thermal mixing catalysts was 330 and 334 m^2/g, respectively. While the specific surface area of commercial γ-Al_2O_3 and amorphous SiO_2 support was 242 and 300 m^2/g, respectively.

2.2. Catalyst characterization

^{29}Si Solid State MAS NMR spectra were recorded on a Bruker Avance 400 MHz spectrometer at 79.49 MHz with 18 s recycle delays and spun at 7 kHz to determine the chemical status of the Si in the silicate framework of catalysts. ^{27}Al Solid State MAS NMR spectra were recorded at 104.3 MHz with 0.3 s recycle delays and spun at 7 kHz to determine the chemical status of aluminum in the silicate framework of catalysts.

The crystallinity of catalysts was measured with a Bruker Advance D8 X-ray powder diffractometer with Cu Kα (λ = 1.5418 Å) radiation as the diffracted monochromatic beam at 40 kV and 40 mA. Nitrogen physisorption analysis was conducted on a Quantachrome Autosorb-1 at 77 K. Before the measurement, the sample was evacuated at 573 K for 3 h. While, the elemental analysis of the catalyst was measured with Agilent 4100 Microwave Plasma – Atomic Emission Spectrometer.

The bulk Si/Al ratio of the HAlMSN was determined by Bruker S4 Explorer X-ray fluorescence spectroscopy (XRF) using Rh as anode target material operated at 20 mA and 50 kV. The analysis showed that the Si/Al ratio of the HAlMSN framework was 18.9.

The morphology and average particle size of the catalyst were estimated from transmission electron microscopy (TEM) images using a JEOL JEM-2100 transmission electron microscope. Prior to the TEM measurements, the powder samples were ground and subjected to ultrasonic treatment in hexane for 10 min. A drop of the suspension was dried on a copper TEM sample grid. A field-emission scanning electron microscope equipped with an energy dispersion X-ray spectrometer (FESEM-EDX) was conducted on FESEM (JEOL JSM-6701 F) to observe the morphology as well as to obtain the elemental analysis of the sample using. Before observation by FESEM-EDX, the sample was coated by Pt using a sputtering instrument.

Fourier Transform Infra Red (FTIR) measurements were carried out using Agilent Carry 640 FTIR Spectrometer. The catalyst was prepared as a self-supported wafer and activated under H_2 stream (F_{H2} = 100 ml/min) at 623 K for 3 h, followed by vacuum at 623 K for 1 h [38]. To determine the acidity of the catalysts, the activated samples were exposed to 2 Torr pyridine at 423 K for 30 min, followed by evacuation at 473 K for 1 h to remove physisorbed pyridine on the samples. In order to study the effect of activation temperature, the HAlMSN was activated at four different temperatures of 473, 523, 573 and 623 K. All spectra were recorded at room temperature. In order to compare the surface coverage of the adsorbed species between different wafer thicknesses, all spectra were normalized using the overtone and combination vibrations of the lattice of MSN between 2200 and 1300 cm^{-1} after activation, particularly the lattice peaks at 1855 cm^{-1} [39]. While, the concentration of pyridine adsorbed on Brønsted and Lewis acid sites was determined based on the report of Emeis [40]. The number of Brønsted and Lewis acid sites was calculated using the integrated molar adsorption coefficient values. The resulting values were ε_{1545} = 1.67 cm/µmol for the band at 1545 cm^{-1} which is characteristic of pyridine on a Brønsted acid sites and ε_{1455} = 2.22 cm/µmol for the 1455 cm^{-1} band of pyridine on a Lewis acid sites.

The thermal analysis measurement was carried out by placing of 10 mg catalyst in an alumina crucible without pressing on the Mettler Toledo TGA/DTG 851 apparatus. The measurement was performed under N_2 flow, by increasing the temperature from ambient temperature to 900 °C at a heating rate of 10 °C/min.

2.3. Catalytic activity

Cumene conversion was carried out under atmospheric pressure in a microcatalytic pulse reactor coupled with an online 6090N Agilent FID/TCD Gas Chromatograph equipped with a VZ-7 packed column. About 0.2 g of catalyst was placed in an OD10 mm quartz glass reactor and subjected to air (F_{Air} = 100 ml/min) stream for 1 h and hydrogen (F_{H2} = 100 ml/min) stream for 4 h at 623 K [41]. A dose of cumene (36 µmol) was injected over the catalyst at the reaction temperature and the products were trapped at 77 K before flushing out to the gas chromatograph. The intervals between each pulse injection were kept constant at 15 min. In order to observe the appropriate condition of cumene conversion, the reaction was done at temperature range of 323–573 K. While, the effect of activation temperature was observed at 473, 523 and 573 K.

The cumene conversion (X_{cumene}) and selectivity of the products (S_i) were calculated according to Eqs. (1) and (2), respectively:

$$X_{Cumene}\ (\%) = \frac{C_{in} - C_{out}}{C_{in}} \times 100 \tag{1}$$

$$S_i\ (\%) = \frac{C_i}{(\sum C_i - C_{out})} \times 100\% \tag{2}$$

where C_{in}, C_{out} and C_i are mole number of cumene in the inlet, outlet, and particular compound, respectively, which calculated based on the Scott hydrocarbon calibration standard gas (Air Liquide America Specially Gases LLC). The i is the number of particular carbon.
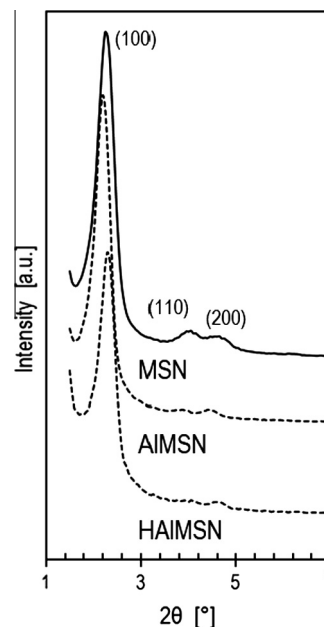

Fig. 1. XRD patterns of MSN, AlMSN and HAlMSN.

3. Results and discussion

3.1. Physical properties of catalysts

The XRD patterns of the MSN and modified MSN samples are shown in Fig. 1. Three intense peaks at $2\theta = 2.30°$, $4.20°$ and $4.70°$ indexed as $(1\,0\,0)$, $(1\,1\,0)$ and $(2\,0\,0)$ were observed for these catalysts [42]. The peaks confirmed the presence of a two-dimensional hexagonal ($p6mm$) structure with d_{100}-spacing of approximately 3.8 nm and an average lattice constant (a_0) of 4.43 nm (Table 1). The presence of a sharp diffraction peak at $2\theta = 2.30°$ illustrates the long-range order of the synthesized MSN. For AlMSN, the intense peak at $2\theta = 2.30°$ shifted to $2.25°$ due to the interaction of a silicon atom with aluminum atom to form framework aluminum which led to an increase in the interplanar spacing of the MSN. The shift-left in peak position may also be caused by the presence of a residual sodium atom which interacted with the Si atom through the O atom [43]. The protonation of AlMSN resulted in the decrease in the intensity of all the peaks and shifted the most intense peak at $2\theta = 2.25°$ to the original position. These changes may be attributed to the partial alteration of the aluminum framework to form extra-framework aluminum and/or the substitution of the sodium atom with a hydrogen atom to form hydroxyl groups.

Table 1 shows the physical properties of the MSN and modified MSN catalysts. The surface area of MSN, AlMSN and HAlMSN are 995, 588 and 639 $m^2\ g^{-1}$, respectively. Alteration of the BET specific surface area may be caused by the change in the pore size distributions and/or the collapsing of the two-dimensional hexagonal structure of the MSN. The grafting of MSN with sodium aluminate has plugged MSN at a pore diameter of around 2–5 nm (Fig. 2). However, the protonation of aluminum-grafted MSN removed partially residual sodium and aluminum inside and/or on the mouth of the pores which reopened the pores of the MSN. This result is in good agreement with the alteration of total pore volume, pore size and pore-wall thickness of the MSN obtained from the BJH method analyses (Table 1). The plugging of the MSN decreased the total pore volume from 0.84 to 0.39 cm^3/g and widened the pore size from 3.37 to 4.00 nm. Whereas, the pore-wall thickness shrank from 1.06 to 0.54 nm due to the widening of the pore size of the MSN. These indicated aluminum and residual sodium placed inside and outside of the pores. Removal of the plug by protonation restored the pore volume, size and wall thickness to almost the original values.

Fig. 2 shows the nitrogen adsorption and desorption isotherms and the pore size distribution of MSN, AlMSN and HAlMSN. The MSN catalyst exhibited isotherm can be classified as Type IV with a Type H4 hysteresis loop which can be attributed to the mesoporous structures of the material, Fig. 2A. The isotherm for MSN shows the characteristics of a sharp inflection of the capillary condensation within uniform pores at P/P_0 of around 0.2–0.4 which indicates the existence of MSN small pore diameter and volume [37]. At a higher relative pressure (P/P_0 between 0.8 and 1.0), a notable increase of adsorbed nitrogen was observed, suggesting an important external surface area contribution. At lower relative pressure ($P/P_0 < 0.2$), gradual and rounded transitions indicated the presence
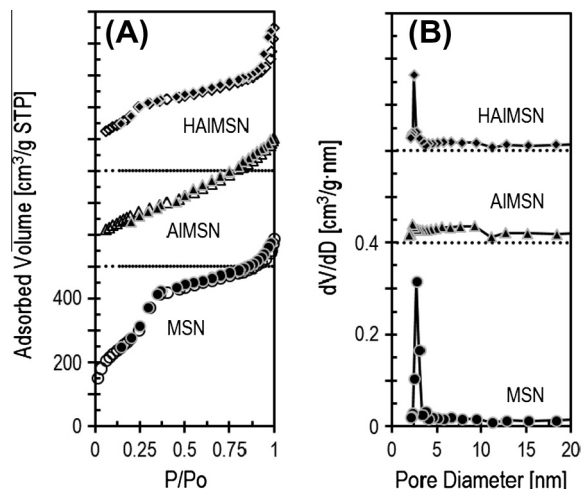

Fig. 2. (A) Nitrogen adsorption and desorption isotherms and (B) pore size distribution for MSN, AlMSN and HAlMSN.

of a small number of non-slit-like micropores, whereas the pore size distribution confirmed the presence of a narrow peak at a pore diameter of around 2–5 nm, Fig. 2B. The aluminum grafting changed the isotherms and pore distribution of MSN in which the inflection isotherms at <0.4 and >0.8 were eliminated. The narrow peak at 2–5 nm was totally eliminated and a small number of pores at a size of around 5–10 nm was formed. The absence of the hysteresis on Al-grafted on MSN showed that the nitrogen adsorption and desorption are from a non-porous surface material. These results verified that the MSN pores may be partially blocked by aluminum. The protonation of AlMSN recovered the isotherm and pore distribution of the MSN. In addition, the inflection of the isotherm at P/P_0 of around 0.8–1.0 increased slightly, indicating the presence of extra-framework aluminum which contributed to the external surface area and the inflection at $P/P_0 < 0.2$ decreased due to the presence of aluminum species inside the microporous MSN.

Similar results were observed on Al loaded on SBA-15 and MCM-41. Kao et al. reported the Al loading of SBA-15 by the post-synthesis method in the Si/Al ratio range of 3–50 [44]. The XRD pattern showed the presence of $(1\,0\,0)$, $(1\,1\,0)$, and $(2\,0\,0)$ diffraction peaks with an ordered hexagonal structure after alumination. The BET results showed a decrease in the surface area from 820 to 620 $m^2\ g^{-1}$ and reduced the pore volume from 1.07 to 0.72 $cm^3\ g^{-1}$ for SBA-15 (Si/Al = 5). In another report, Trong On et al. immobilized Al into an MCM-41 mesoporous framework with an Si/Al ratio of 33 [45]. The X-ray diffraction result exhibited that the ordered hexagonal structure of the parent MCM-41 did not change and showed a d-spacing of ca. 40 and 41 Å for MCM-41 and Al-MCM-41, respectively. Both samples represented narrow pore size distributions of around 28 Å with surface areas of 1050 and 815 $m^2\ g^{-1}$ for MCM-41 and Al-MCM-41, respectively.

The morphology of the MSN was observed using FESEM and TEM images. Fig. 3A–C shows the agglomeration of the MSN and modified MSN as fairly uniform spherical particles with particle size of 70–120 nm. The two-dimension hexagonal mesostructure was further confirmed by TEM analysis (Fig. 3D–F). The TEM images and their diffraction patterns (inset figures) clearly determined well-ordered pores with parallel and cylindrical channels and honeycomb structures, which indicates a 2D hexagonal $p6mm$ mesostructure for all catalysts [45]. These results are in accordance with those measured from the low-angle XRD patterns and N_2 adsorption–desorption analysis.

Fig. 4 shows the peaks of ^{29}Si MAS NMR spectra which the pure MSN showing an intense peak centered at -111.7 ppm, which was

Table 1
Physical properties of MSN, AlMSN and HAlMSN.

Sample	d_{100} (nm)	a_0 (nm)	S (m²/g)	V_p (cm³/g)	W (nm)	t (nm)
MSN	3.84	4.43	995	0.84	3.37	1.06
AlMSN	3.92	4.53	588	0.39	4.00	0.53
HAlMSN	3.76	4.34	639	0.54	3.38	0.96

d_{100}, d-value 100 reflections; a_0, pore center distance is equal to $d_{100} \times 2/\sqrt{3}$; S, BET surface area (m²/g) obtained from N_2 adsorption; V_p, total pore volume (ml/g); W, pore size (nm) obtained from BJH method; t, pore-wall thickness is equal to $a_0 - W$.

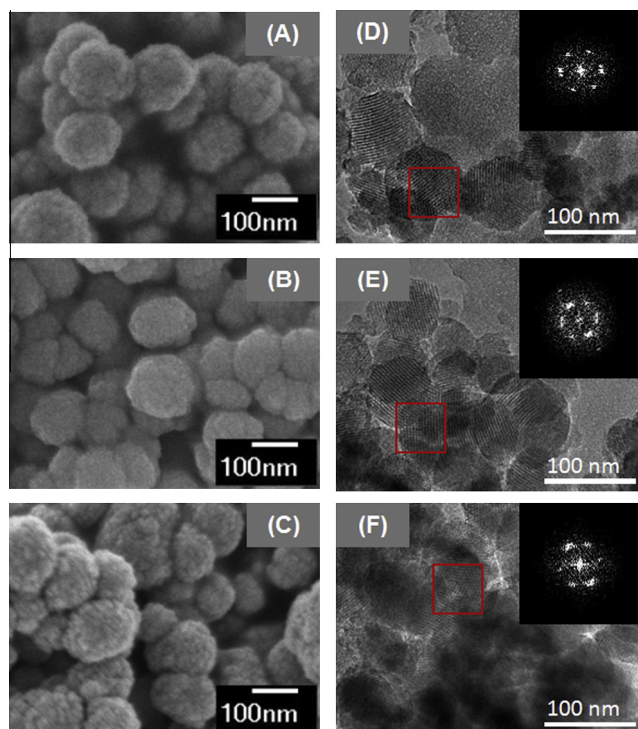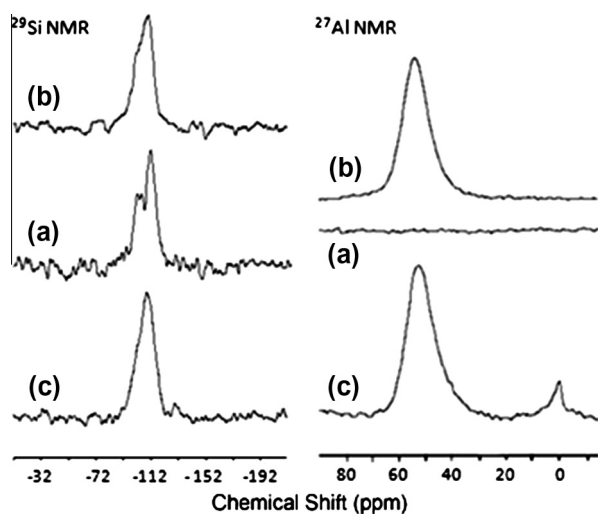**Fig. 3.** FESEM (left) and TEM (right) images of (A and D) MSN, (B and E) AlMSN and (C and F) HAlMSN.

Fig. 4. ^{29}Si and ^{27}Al Solid State NMR for (a) MSN, (b) AlMSN and (c) HAlMSN.

assigned to ($\equiv$SiO)$_4$Si. The shoulder peaks centered at −104.2 and −99.9 ppm were assigned to ($\equiv$SiO)$_3$Si— and ($\equiv$SiO)$_2$Si=, respectively [46,47]. The aluminum grafting and protonation of MSN partially eliminated the peaks corresponding to ($\equiv$SiO)$_3$Si— and slightly intensified the peaks corresponding to ($\equiv$SiO)$_2$Si=. In ^{27}Al MAS NMR spectra, no peak was observed for pure MSN, while the peak corresponding to 4-coordinated aluminum at approximately 53 ppm was observed for both AlMSN and HAlMSN [30]. This result indicates that the grafting of MSN with sodium aluminate led to the formation of an aluminosilicate framework. The protonation of Al-grafted on MSN resulted in the appearance of a small peak corresponding to 6-coordinated (extra-framework) aluminum at approximately 0 ppm, which showed that a small part of the aluminum dislodged from the aluminosilicate frame-

work [30,48]. Nevertheless, most of the aluminum species remained in the 4-coordinated (framework) structure, which is promising for catalytic reactions.

Chen et al. described the synthesis of Al-MCM-41 by the grafting method in various Si/Al ratios showing two types of Al structure in the MCM-41 frameworks [30]. ^{27}Al MAS NMR spectra with the signals at 53 and 0 ppm were observed indicating the presence of four- and six-coordinated Al in the Al-MCM-41 framework. Hu et al. reported that the ^{27}Al MAS NMR spectrum of Al-SBA-15 in the different Si/Al ratios showed a strong single resonance at around 54 ppm, which was ascribed to tetrahedral framework aluminum formed in the mesoporous wall of the materials, and that the octahedral Al structure appeared at around 0 ppm [48].

Fig. 5 shows the FTIR spectroscopy of MSN and modified MSN. The pure MSN have an electrically neutral framework and do not have Brønsted acid sites. Thus, the silanol groups of MSN that appear at the range of 3800–3500 cm^{-1} in Fig. 5A and B do not show the acidic properties. The sharp band at 3740 cm^{-1} is assigned to the non-acidic terminal silanol groups ($\equiv$SiOH) located on the external surface of the parent mesoporous (Fig. 5A) [49]. Another non-acidic OH groups on structural defects and/or vicinal hydroxyl groups were observed at 3550, 3625, 3635 and 3655 cm^{-1} (Fig. 5B) [39]. The aluminum grafting decreased the H-bonds of the hydroxyl groups on the MSN and simultaneously decreased the intensity of non-acidic hydroxyl groups corresponding to the terminal silanol groups, hydroxyl groups on structural defects and vicinal hydroxyl groups. The decreases may be due to the formation of the aluminosilicate framework and the interaction of residual sodium with the Si atom through the O atom. However, the intensity of the band at 3740 cm^{-1} increased to almost the original intensity and the new peak at 3745 cm^{-1} was developed after protonation indicating the formation of geminal silanol groups due to the dislodging of aluminum from the aluminosilicate framework. There are no significant differences in the band intensities in the region of 3740 cm^{-1} for the pure MSN and HAlMSN samples, which reveals that they have a comparable primary particle size and have no significant differences in the d_{100}-spacing or pore diameters [50]. In addition, the protonation of Al-grafted MSN has eliminated small peaks at 3655 and 3635 cm^{-1}, and developed new peaks at 3605 and 3645 cm^{-1} corresponding to the bridging silanol groups (Si(OH)Al) and Al^{3+} cations in extra-framework Al-oxide clusters.

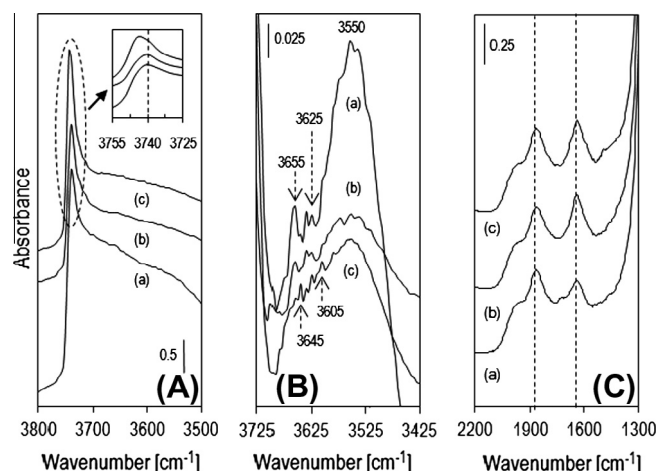**Fig. 5.** FTIR spectra of MSN types for (A) hydroxyl groups stretching region at 3500–3800 cm^{-1}, (B) Baseline correction of hydroxyl stretching region at 3425–3725 cm^{-1} and (C) lattice stretching regions at 1300–2200 cm^{-1}. (a) MSN, (b) AlMSN and (c) HAlMSN.

The vibrational lattice stretching frequency of these catalysts in the region of 2200–1550 cm^{-1} are shown in Fig. 5C. The primary bands were observed at 1855 and 1640 cm^{-1}, which may correspond to the Si atom connected to another 4Si atom through the O atom, and the Si atom connected to another Si and/or an H atom through the O atom. The aluminum grafting and protonation eliminated the vibrational band at 1720 cm^{-1} and intensified the band 1640 cm^{-1}, which may correspond to the decrease in the structural defects and increase in the concentration of the Si atom connected to an aluminum or H atom through the O atom.

3.2. Nature and strength of acidity

The nature of the acid sites in the catalysts was qualitatively probed by pyridine adsorption monitored by IR spectroscopy. Fig. 6A shows the IR spectra of the adsorbed pyridine on the activated MSN, AlMSN, HAlMSN catalysts in the region of 1600–1400 cm^{-1} and Fig. 6B shows the pyridine adsorbed IR spectra of the HAlMSN catalyst activated at different temperatures of 473, 523, 573 and 623 K. Pyridine was adsorbed at 423 K for 30 min, followed by outgassing at 473 K for 1 h.

Fig. 6A shows the presence of absorbance bands at 1455–1445 cm^{-1} attributed to Lewis acid sites and at 1545 cm^{-1} attributed to Brønsted acid sites, while, the absorbance band at around 1495 cm^{-1} is related to the combination of Lewis and Brønsted acid sites [49]. The pure MSN possesses only strong Lewis acid sites at 1445 cm^{-1} which corresponding to the presence of electron pair acceptor sites from SiOH groups. The aluminum grafting slightly increased the Lewis acidity of the MSN due to the presence of relatively weak Lewis acid sites from alkali cations. While the protonation of aluminum-grafted MSN generated strong Brønsted acid sites which may correspond to the formation of acidic MSN-OH groups (OH groups which bound the Si or Al in the framework) [51,52] and/or bridging hydroxyl (SiO(H)Al) groups. The small shift-left in the peak of the Lewis acid sites at 1445–1455 cm^{-1} may be related to the alteration of the acidic center from the SiOH groups and/or alkali cations to the stronger Lewis acid sites corresponding to the extra-framework aluminum which may be in the form of Al(OH)$_3$ and/or Al(OH)$^{2+}$ [41,51]. Fig. 6B shows the effect of activation temperature on the intensity of both Lewis and Brønsted acid sites. The ratio of Lewis to Brønsted acid sites increased with an increase in the activation temperature due to the increase in the dehydration and/or dehydroxylation process and removal of acidic OH groups leaving Lewis acid sites. Fig. 6C shows the acid strength of the commercial γ-Al$_2$O$_3$, amorphous SiO$_2$ and mixed γ-Al$_2$O$_3$–SiO$_2$. No-Brønsted acid sites were observed on commercial γ-Al$_2$O$_3$, amorphous SiO$_2$ and simple mixed γ-Al$_2$O$_3$–SiO$_2$. While thermal mixed γ-Al$_2$O$_3$–SiO$_2$ possessed small amount of Brønsted acid sites indicating the interaction of γ-Al$_2$O$_3$ and SiO$_2$ led to form surface hydroxyl groups. In contrast, all samples possessed relatively weak Lewis acid sites due to the presence of cationic metal centers in the metal oxides or mixed metal oxides. The absence of the strong Brønsted and Lewis acid sites on the mixed γ-Al$_2$O$_3$–SiO$_2$ may be related to the absence of aluminosilicate framework. In general, the acidity of HAlMSN is much higher than that of SiO$_2$ based catalysts in this experiment. And it should be noted that the acidity of HAlMSN is comparable or higher than common solid acid catalysts such as HZSM-5, HY and AlMCM-41 reported by several research groups as listed in Table 2 [37,44].

3.3. Cumene conversion

The catalytic activities of MSN and modified MSN were evaluated with respect to the cumene conversion at a temperature range of 323–573 K in a microcatalytic pulse reactor under hydrogen or nitrogen carrier gas. The products were composed of propylene (C$_3$), benzene (C$_6$), toluene (C$_7$), α-methylstyrene (C$_9$) and trace amount of heavy hydrocarbon ($\geqslant$C$_{10}$). The high activity of cumene conversion over HAlMSN was due to the presence of molecular hydrogen and strong Lewis acid sites in which the strong Lewis acid sites acts as active site for the generation of protonic acid sites from molecular hydrogen. Then, the formed protonic acid sites facilitated the cracking of cumene producing propylene, benzene and small amount of toluene. In addition to the active sites for formation of protonic acid sites, the strong Lewis acid sites enhanced the cumene conversion via a dehydrogenation process producing α-methylstyrene [53–55]. The dehydrogenation of cumene over Lewis acid sites was predominant in the temperature range of 323–573 K. In a pulse microcatalytic reactor, it is plausible that the equilibrium of cumene conversion to α-methylstyrene shifted for increasing of α-methylstyrene product, leaving the hydrogen which escaped from the reaction phase by column effect. In agreement with this result, Corma et al. reported that the presence of Brønsted acid sites in the cumene cracking was responsible for the formation of carbenium ion which led to form C$_3$ and C$_6$ [56]. While the presence of strong Lewis acid sites accelerated the hydride transfer which enhanced the formation of α-methylstyrene (C$_9$). Bradely and Kydd reported a cracking reaction of isopropylbenzene with an alumina supported gallium catalyst for the production of propylene and α-methylstyrene through solid catalyzed dehydrogenation and cracking reactions [53]. Cumene dehydrogenation has also been explored over complex-derived Cr- and Fe–Cr-pillared clays in which the products of benzene and propene was formed at low temperature, and the α-methylstyrene was observed at higher temperatures [55].

Fig. 7 shows the activity of HAlMSN in cumene catalytic conversion in the presence of hydrogen and nitrogen carrier gases. The activity of HAlMSN increased with increase in the reaction temperature in which the extensive increase was observed in the presence of hydrogen (Fig. 7A). At 523 K, the conversion of cumene reached 55% in the presence of hydrogen which is about two-fold higher than in the presence of nitrogen carrier gas. The high activity may be due to the role of molecular hydrogen as active sites for the reaction and/or the removal of coke deposits by the hydrogenation process assisted by the presence of strong Lewis acid sites [57]. The detail product distribution of cumene conversion under hydrogen and nitrogen carrier gases is listed in Table 3. At low
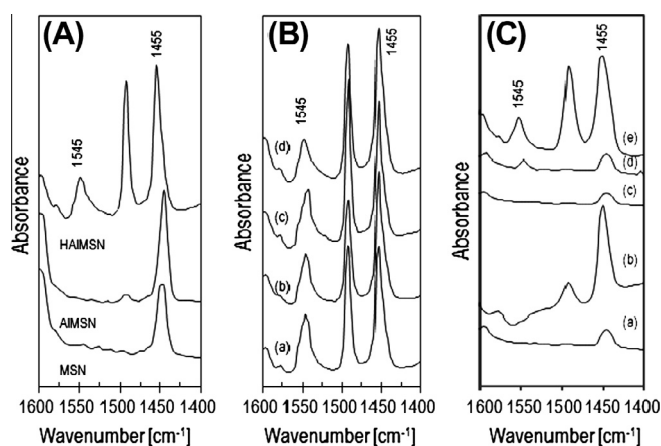

Fig. 6. (A) FTIR spectra of pyridine for MSN, AlMSN and HAlMSN. The samples were activated under H$_2$ stream (F_{H2} = 100 ml/min) at 623 K for 3 h, followed by vacuum at 623 K for 1 h. Pyridine was adsorbed at 423 K for 30 min, followed by outgassing at 473 K for 1 h. (B) Variations of pyridine adsorbed FTIR for HAlMSN at different activation temperatures, (a) 473, (b) 523, (c) 573 (d) 623 K. Pyridine was adsorbed at 423 K for 30 min, followed by outgassing at 473 K for 1 h. (C) FTIR spectra of pyridine for (a) amorphous SiO$_2$, (b) commercial γ-Al$_2$O$_3$, (c) physical mixed γ-Al$_2$O$_3$–SiO$_2$, (d) thermal mixed γ-Al$_2$O$_3$–SiO$_2$ and (e) HAlMSN.

Table 2
Concentration of Brønsted and Lewis acid sites for MSN, AlMSN, HAlMSN and other type of solid acid catalysts.

Catalyst	Brønsted acid sites (μmol g^{-1})	Lewis acid sites (μmol g^{-1})	Ref.
MSN	0	80	This study
AlMSN	9	107	This study
HAlMSN	96	189	This study
Commercial γ-Al$_2$O$_3$	0	59	This study
Amorphous SiO$_2$	0	12.3	This study
Physically mixed γ-Al$_2$O$_3$–SiO$_2$ (Si/Al = 20)	0	16	This study
Thermal mixed γ-Al$_2$O$_3$–SiO$_2$ (Si/Al = 20)[a]	21	32	This study
HZSM-5 (Si/Al = 23)	88	30	[39]
HY (Si/Al = 22)	170	36	[39]
NaY	60	81	[39]
AlMCM-41 (Grafting)	0.5	28.6	[40]
AlMCM-41 (Sol–Gel)	37.7	78.9	[40]

[a] Prepared by mixing of γ-Al$_2$O$_3$ and SiO$_2$ (Si/Al = 20) in a 5% NaOH solution at 353 K for 10 h, followed by dried at 383 K overnight and calcinations at 823 K for 3 h.
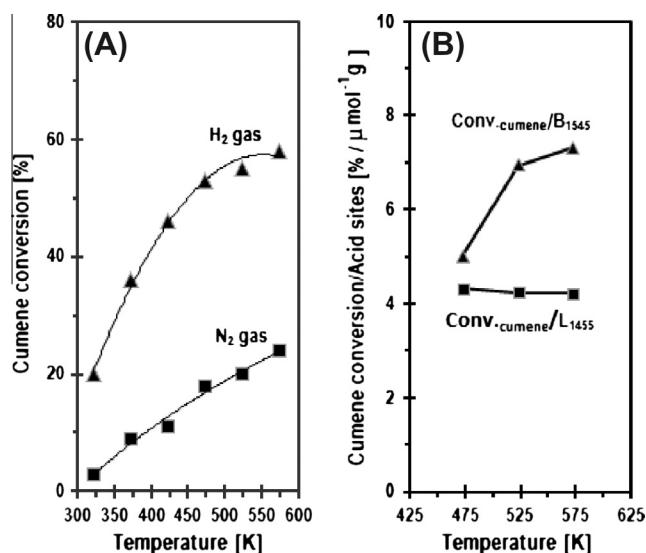
Fig. 7. (A) Conversion of cumene over HAlMSN at different reaction temperatures in the presence of hydrogen and nitrogen gases. (B) The relation between cumene conversion with the number of acidic sites at 473–573 K.

temperature (<373 K), only α-methylstyrene and higher hydrocarbon ($\geqslant$C$_{10}$) were observed under both hydrogen and nitrogen carrier gases. The α-methylstyrene showed a higher selectivity than higher hydrocarbon ($\geqslant$C$_{10}$) showing the cumene conversion may be proceeded via a dehydrogenation followed by a dimerization-cracking process. No lower hydrocarbon (C$_3$ and C$_6$) products were observed in this temperature range indicating the protonic acid sited and/or the reaction temperature were not enough to initiate the cracking process. It should be noted that the conversion was low at this temperature range, particularly for conversion under the nitrogen carrier gas which showing that the conversion

occurred only on the Lewis acid sites. The number of both α-methylstyrene and heavy hydrocarbon decreased with increase in the temperature due to the thermal and/or acid-catalyzed cracking processes were taking place. A wide distribution of products was obviously observed at relatively high temperatures. In general, lower hydrocarbons were formed at a higher temperature reaction and tended to increase with increase in the reaction temperature with a simultaneous decrease in the higher hydrocarbon products. In the presence of hydrogen, α-methylstyrene and higher hydrocarbon ($\geqslant$C$_{10}$) markedly decreased at high temperature and the distribution of C$_1$ and C$_6$ products increased. Contrarily, in the presence of nitrogen gas, the α-methylstyrene did not change much showing that the dehydrogenation of cumene strongly depends on the Lewis acid sites, but the higher hydrocarbon ($\geqslant$C$_{10}$) markedly decreased in simultaneous increase of lower hydrocarbon at high temperature indicating the thermal cracking was taking place on the acidic sites.

The alteration of the products distribution caused by the presence of hydrogen and the variations of the reaction temperatures verified the promotion effect of hydrogen in the cumene conversion through a hydrogen spillover phenomena [58,59]. The role of acidic sites was strongly evidenced by the activity–acidic sites relationship in Fig. 7B. The ratio of the conversion to the concentration of Lewis acid sites did not change much in the temperature range of 473–573 K, while the ratio to the concentration of the permanent Brønsted acid sites markedly altered. This result indicated that the cumene conversion is directly correlated with the concentration of Lewis acid sites in which the Lewis acid sites have important roles in the stabilization of the formed protons and facilitating the dehydrogenation process. Thus, on the basis of the conversion results, the HAlMSN owes its activity primarily to a number of Lewis acid sites. It is also suggested that the presence of permanent Brønsted acid cannot be directly associated with the cumene conversion acitivity over HAlMSN. In fact, the conversion was low for the reaction in the absence of molecular hydrogen. It should be noted too that the alteration of the two-dimensional hexagonal

Table 3
Product distribution of cumene conversion over HAlMSN in the presence of hydrogen and nitrogen carrier gases at different temperatures. A number in the parentheses indicated the product for the cumene conversion in the presence of nitrogen.

React. temp. (K)	323	373	423	473	523	573
Cumene conversion (%)	20(3)	35.5(9)	46(11)	53(18)	55(20)	58(24)
Selectivity (%)						
Propylene	0(0)	3.1(0.6)	9.5(2.8)	14.3(4.3)	19.4(11.4)	20(15.2)
Benzene	0(0)	1(0.2)	1.3(0.9)	4.8(2.9)	34.1(6.8)	37(10.2)
Toluene	0.1(0.4)	0.3(0.6)	0.6(2.2)	0.7(2.8)	2.4(6.9)	6(6.8)
α-Methylstyrene	85(73.8)	84.3(73.4)	82.9(73.1)	76.9(72.6)	43.7(70.6)	37(67.8)
$\geqslant$C$_{10}$	14.9(25.8)	11.3(25.2)	5.7(21)	3.3(17.4)	0.4(4.3)	0(0)

(p6mm) structure of the MSN, pore size and surface area did not diretly affect the activity of the catalysts. Although, the MSN and AlMSN possessed higher crystallinity, surface area, average pore size and total pore volume than that of HAlMSN, the activity of MSN and AlMSN was far lower than HAlMSN, Table 4. Therefore, it is suggested that the relation between the structure of HAlMSN and its activity is not appreciable to the present study, although certain value of pore size, surface area and crystallinity is necessary to accelerate the reaction or diffusion of the reactant and products.

Table 4 shows the comparison study of cumene conversion over several types of solid catalysts such as Al-SBA, Al-MS-20, Al-MCM-41, commercial γ-Al$_2$O$_3$, amorphous SiO$_2$ and mixed γ-Al$_2$O$_3$–SiO$_2$ [35,44,48,52]. The results showed that the activity of HAlMSN is comparable or better than other type of solid acid catalysts. The high activity of HAlMSN in the cumene conversion most probably is due to the presence of extra-framework aluminum which generates strong Lewis acid sites and small particle of MSN which provides more interaction between active sites and reactant or hydrogen carrier gas.
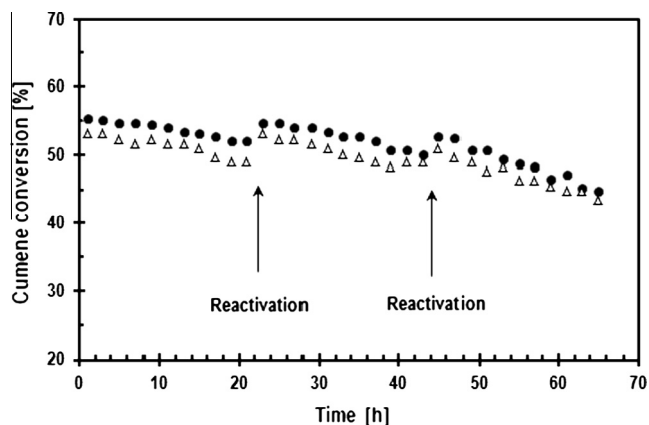
3.4. Stability testing

Fig. 8 shows the stability of HAlMSN in the cumene conversion at 473 and 523 K. The reactions were undertaken for more than 60 h with intervals between each pulse injection kept constant at 15 min. In both conditions, the activity of HAlMSN decreased slightly with the reaction temperature. The activity recovered slightly after the reactivation of the catalyst by heating at 623 K under oxygen stream for 1 h, followed by hydrogen stream for 2 h at 623 K. However, the activity of catalyst and subsequently coke formation is larger at the high temperatures, the results show that the trend of reactivation processes are similar at 473 and 523 K. The conversions of cumene reached 53% and 55% at 473 and 523 K, respectively. However the activity slightly decreased with the reaction time. The catalyst restores its activity after reactivation process and reaches close to the initial activity. It is plausible that the formation of coke and/or the collapsing of the hexagonal structure resulted in the deactivation of HAlMSN. The small slopes of the deactivation processes at 473 and 523 K indicate that HAlMSN is a stable catalyst and low coke deposit and/ or the structure collapsing occur during the hydrocracking reactions. XRD results (not shown) indicated that there is no significant change after the reaction; however, coke deposits were observed on the used HAlMSN as illustrated in Fig. 9. The strong distinctive band corresponds to the vibration of C=C observed at 1645 cm^{-1}, which may be related to the presence of olefinic species [60]. In addition, two weak bands observed at 2860 and 2930 cm^{-1} confirmed the presence of the C—H stretching vibration, which may be related to the aliphatic hydrocarbons.

Fig. 8. Stability of HAlMSN in the cumene conversion at 473 ($\triangle$) and 523 K ($\bullet$) in the presence of hydrogen gas. The reactivations were done at 623 K under oxygen stream for 1 h, followed by hydrogen stream for 2 h.
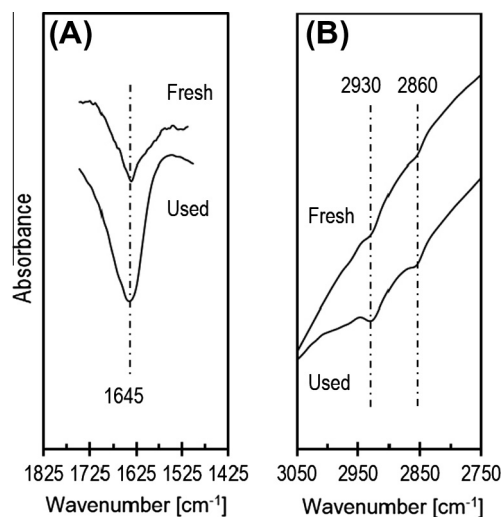
Fig. 9. FTIR spectra of (a) fresh HAlMSN and (b) used HAlMSN in the (A) C=C and (B) C—H stretching regions. Cumene conversion was done at 573 K in the presence of hydrogen stream.

Thermal gravimetric and differential thermogravimetric analyses of fresh and used HAlMSN are shown in Fig. 10. Almost similar results were obtained for both catalysts. Thermal gravimetric results showed the mass change below 350 °C, while the differential thermogravimetric results showed very weak endothermic peaks centered at 565 °C. These results indicated the desorption of hydroxyl groups or/and desorption/decomposition of silanol

Table 4
The activity of cumene conversion over MSN, AlMSN, HAlMSN and other type of solid acid catalysts in the presence of hydrogen gas.

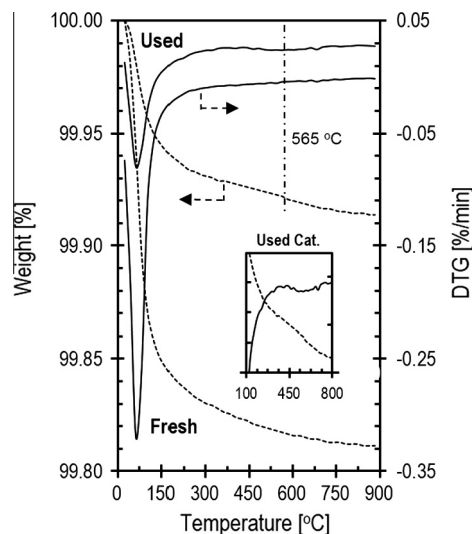| Catalyst	Cumene conversion (%)	Temperature (K)	Ref.
MSN	1.4	523	This study
AlMSN	9.8	523	This study
HAlMSN	55	523	This study
Commercial γ-Al$_2$O$_3$	Trace	523	This study
Amorphous SiO$_2$	Trace	523	This study
Physically mixed γ-Al$_2$O$_3$–SiO$_2$	Trace	523	This study
Thermal mixed γ-Al$_2$O$_3$–SiO$_2$	Trace	523	This study
Al-SBA-10	43.2	523	[31]
Al-SBA-20	17.1	523	[31]
Al-MCM-41(Si/Al = 11.8)	2.5	573	[44]
Al-MCM-41(Si/Al = 20)	13.5	573	[45]
Al-MS-20	4.0	523	[48]

Fig. 10. Thermal analyses of (a) fresh and (b) used HAlMSN; TGA (dotted lines) and DTG (true lines). Inset figure is the magnification of used catalyst in the temperature range of 100–800 °C.

groups on the framework to produce water and/or Si=O$^-$ groups [42]. The further heating up to 900 °C decreased the mass of both samples gradually. No distinction DTG peak was observed for fresh catalyst indicating there is no phase change was observed in the temperature range of 350–900 °C. The mass change in this temperature range may be related to the desorption of hydroxyl groups inside the channel or pore of the sample.

The formation of the small coke on the catalyst is in agreement with the catalytic testing and FTIR results. The activity of the catalyst decreased to some extent after 20 h of the reaction and the activity restore to its original after reactivation or removal of coke. While the used catalyst possessed C=H stretching vibration at 1930 and 2860 cm^{-1} indicating the presence of coke.

4. Conclusion

The hexagonal structure of the MSN based solid acid catalyst was prepared by the sol–gel method, followed by aluminum grafting and protonation. The XRD, TEM and N$_2$ physisorption results confirmed the hexagonal ordered structure with pore diameter of 3.4–4.0 nm and surface area of 588–995 m^2/g, whereas the solid state NMR and IR results confirmed that the aluminum grafting and protonation form framework and extra-framework aluminums, which led to the generation of strong Brønsted and Lewis acidic sites for which the pyridine probe molecule remained after outgassing at 473 K. HAlMSN in particular possesses extra-framework aluminum, which generates strong Lewis acidic sites centered on Al(OH)$_3$ and/or Al(OH)$^{2+}$.

The catalytic testing was undertaken on cumene conversion under a hydrogen and nitrogen atmosphere. The HAlMSN exhibited high activity in the presence of hydrogen, whereas low activity was observed for MSN and AlMSN regardless of the carrier gas used. This result indicated the indispensability of hydrogen gas and strong Lewis acid sites in the cumene conversion over HAlMSN. A small deactivation was observed during the reaction due to the formation of coke deposits on the surface. The activity was recovered slightly by heating under oxygen and hydrogen at 623 K. It is noteworthy that the high activity of HAlMSN in cumene conversion was still observed after 60 h in the presence of hydrogen.

The conversion of cumene reached 55% at 523 K in the presence of hydrogen, which is more than two-fold higher than in the presence of nitrogen carrier gas. The product distribution showed the predominant products of α-methylstyrene at all reaction temperatures. In a pulse reactor, the conversion of cumene to α-methylstyrene exceeded the equilibrium which releasing hydrogen from the raction system. Whereas, the propylene, benzene and toluene products were observed at a higher reaction temperature. It is plausible that the conversion of cumene proceeds in one of two ways: cracking to propylene, benzene, toluene, and dehydrogenation to α-methylstyrene. The first route was catalyzed by H$_2$-originated protonic acid sites via a cracking/dealkylation and the second route was catalyzed by Lewis acid sites via dehydrogenation. On the basis of the conversion results, the HAlMSN owes its activity primarily to a number of Lewis acid sites, and contrarily, the presence of permanent Brønsted acid cannot be directly associated with the cumene conversion activity over HAlMSN. We believe that this new HAlMSN and reaction presented here are useful for studying of numerous hydrocarbon reactions and the consideration as a new method for the production of α-methylstyrene over solid acid catalysts.

References

[1] X. Wei, W. Wang, J. Xiao, L. Zhang, H. Chen, J. Ding, Hierarchically porous aluminosilicates as the water vapor adsorbents for dehumidification, Chem. Eng. J. 228 (2013) 1133–1139.
[2] Q. Zhao, Y. Shen, Q. Wang, J. Tian, X. Zhou, T. Jiang, A comparative investigation on the catalytic activity of H-Al-MCM-48 and H-Zr-MCM-48 mesoporous molecular sieve on alkylation of phenol with *tert*-butyl alcohol, Chem. Eng. J. 230 (2013) 124–132.
[3] R.K.S. Almeida, Cléo T.G.V.M.T. Pires, C. Airoldi, The influence of secondary structure directing agents on the formation of mesoporous SBA-16 silicas, Chem. Eng. J. 203 (2012) 36–42.
[4] C. Liang, M.C. Wei, H.H. Tseng, E.C. Shu, Synthesis and characterization of the acidic properties and pore texture of Al-SBA-15 supports for the canola oil transesterification, Chem. Eng. J. 223 (2013) 785–794.
[5] L.Y. Lin, H. Bai, Aerosol processing of low-cost mesoporous silica spherical particles from photonic industrial waste powder for CO$_2$ capture, Chem. Eng. J. 197 (2012) 215–222.
[6] H. Jin, M.B. Ansari, E.Y. Jeong, S.E. Park, Effect of mesoporosity on selective benzylation of aromatics with benzyl alcohol over mesoporous ZSM-5, J. Catal. 291 (2012) 55–62.
[7] C.J. Van Oers, K. Góra-Marek, K. Sadowska, M. Mertens, V. Meynen, J. Datka, P. Cool, In situ IR spectroscopic study to reveal the impact of the synthesis conditions of zeolite β nanoparticles on the acidic properties of the resulting zeolite, Chem. Eng. J. 237 (2014) 372–379.
[8] Z. Qu, Y. Bu, Y. Qin, Y. Wang, Q. Fu, The effects of alkali metal on structure of manganese oxide supported on SBA-15 for application in the toluene catalytic oxidation, Chem. Eng. J. 209 (2012) 163–169.
[9] J. Gu, W. Fan, A. Shimojima, T. Okubo, Organic-inorganic mesoporous nanocarriers integrated with biogenic ligands, Small 3 (2007) 1740–1744.
[10] J.N. Kondo, S. Yang, S. Inagaki, Q. Zhu, K. Domen, In situ infrared study of *n*-heptane isomerization over Pt/H-beta zeolites, J. Catal. 248 (2007) 53–59.
[11] M. Manzano, V. Aina, C.O. Are, F. Balas, V. Cauda, M. Colilla, M.R. Delgado, M. Vallet-Reg, Studies on MCM-41 mesoporous silica for drug delivery: Effect of particle morphology and amine functionalization, Chem. Eng. J. 137 (2008) 30–37.
[12] C. Sealy, Nanoparticle drug delivery system targets damaged arteries, Nano Today 5 (2010) 79–80.
[13] C. Han, H. Li, H. Pu, H. Yu, L. Deng, S. Huang, Y. Luo, Synthesis and characterization of mesoporous alumina and their performances for removing arsenic(V), Chem. Eng. J. 217 (2013) 1–9.
[14] A.H. Karim, A.A. Jalil, S. Triwahyono, S.M. Sidik, N.H.N. Kamarudin, R. Jusoh, N.W.C. Jusoh, B.H. Hameed, Amino modified mesostructured silica nanoparticles for efficient adsorption of methylene blue, J. Colloid Interface Sci. 386 (2012) 307–314.

[15] N. Sapawe, A.A. Jalil, S. Triwahyono, One-pot electro-synthesis of ZrO–ZnO/HY nanocomposite for photocatalytic decolorization of various dye-contaminants, Chem. Eng. J. 225 (2013) 254–265.

[16] R. Mokaya, Al_x^{n+}-grafted MCM-41 catalysts: probing the influence of temperature on the alumination process, J. Catal. 193 (2000) 103–107.

[17] C.T. Kresge, M.E. Leonowicz, W.J. Roth, J.C. Vartuli, J.S. Beck, Ordered mesoporous molecular sieves synthesized by a liquid–crystal template mechanism, Nature 6397 (1992) 710–712.

[18] Z. Qin, B. Shen, Z. Yu, F. Deng, L. Zhao, S. Zhou, D.Y.X. Gao, B. Wang, H. Zhao, H. Liu, A defect-based strategy for the preparation of mesoporous zeolite Y for high-performance catalytic cracking, J. Catal. 298 (2013) 102–111.

[19] S.P. Naik, S.P. Elangovan, T. Okubo, I. Sokolov, Morphology control of mesoporous silica particles, J. Phys. Chem. C 111 (2007) 11168–11173.

[20] V.V. Ordomsky, I.I. Ivanova, E.E. Knyazeva, V.V. Yuschenko, V.I. Zaikovskii, Cumene disproportionation over micro/mesoporous catalysts obtained by recrystallization of mordenite, J. Catal. 295 (2012) 207–216.

[21] S. Triwahyono, A.A. Jalil, M. Malik, Generation of protonic acid sites from pentane on the surfaces of Pt/SO_4^{2-}–ZrO_2 and Zn/H-ZSM5 evidenced by IR study of adsorbed pyridine, Appl. Catal. A 372 (2010) 90–93.

[22] S. Triwahyono, A.A. Jalil, R.R. Mukti, M. Musthofa, N.A.M. Razali, M.A.A. Aziz, Hydrogen spillover behavior of Zn/HZSM-5 showing catalytically active protonic acid sites in the isomerization of *n*-pentane, Appl. Catal. A 407 (2011) 91–99.

[23] R.V. Grieken, J.M. Escola, J. Moreno, R. Rodríguez, Direct synthesis of mesoporous M-SBA-15 (M = Al, Fe, B, Cr) and application to 1-hexene oligomerization, Chem. Eng. J. 155 (2009) 442–450.

[24] H.D. Setiabudi, A.A. Jalil, S. Triwahyono, N.H.N. Kamarudin, R.R. Mukti, IR study of iridium bonded to perturbed silanol groups of Pt-HZSM5 for *n*-pentane isomerization, Appl. Catal. A 417–418 (2012) 190–199.

[25] M. Hussain, D. Fino, N. Russo, Development of modified KIT-6 and SBA-15-spherical supported Rh catalysts for N_2O abatement: from powder to monolith supported catalysts, Chem. Eng. J. (2013). http://dx.doi.org/10.1016/j.cej.2013.06.032.

[26] T. Li, S.T. Wong, M.C. Chao, H.P. Lin, C.Y. Mou, S. Cheng, W/Zr mixed oxide supported on mesoporous silica as catalyst for *n*-pentane isomerization, Stud. Surf. Sci. Catal. 146 (2003) 569–572.

[27] J.H. Wang, C.Y. Mou, Characterizations of aluminum-promoted sulfated zirconia on mesoporous MCM-41 silica: butane isomerization, Micropor. Mesopor. Mater. 110 (2008) 260–270.

[28] J.H. Wang, C.Y. Mou, Alumina-promoted mesoporous sulfated zirconia: a catalyst for *n*-butane isomerization, Appl. Catal. A 286 (2005) 128–136.

[29] R. Ryoo, C.H. Ko, R.F. Howe, Imaging the distribution of framework aluminum in mesoporous molecular sieve MCM-41, Chem. Mater. 9 (1997) 1607–1613.

[30] L.Y. Chen, Z. Ping, G.K. Chuah, S. Jaenicke, G. Simon, A comparison of post-synthesis alumination and sol–gel synthesis of MCM-41 with high framework aluminum content, Micropor. Mesopor. Mater. 27 (1999) 231–242.

[31] S.K. Jana, H. Takahashi, M. Nakamura, M. Kaneko, R. Nishida, H. Shimizu, T. Kugita, S. Namba, Aluminum incorporation in mesoporous MCM-41 molecular sieves and their catalytic performance in acid-catalyzed reactions, Appl. Catal. A 245 (2003) 33–41.

[32] T. Kugita, S.K. Jana, T. Owada, N. Hashimoto, M. Onaka, S. Namba, Mesoporous Al-containing MCM-41 molecular sieves: highly active catalysts for Diels–Alder reaction of cyclopentadiene with α,β-unsaturated aldehydes, Appl. Catal. A 245 (2003) 353–362.

[33] H.M. Kao, H.M. Wu, Y.W. Liao, A.S.T. Chiang, Aluminosilicate MCM-48 mesostructures assembled from dried zeolite precursors and Gemini surfactant, Micropor. Mesopor. Mater. 86 (2005) 256–267.

[34] G.M. Kumaran, S. Garg, K. Soni, M. Kumar, J.K. Gupta, L.D. Sharma, K.S.R. Rao, G.M. Dhar, Synthesis and characterization of acidic properties of Al-SBA-15 materials with varying Si/Al ratios, Micropor. Mesopor. Mater. 114 (2008) 103–109.

[35] Y.H. Yue, A. Gedeon, J.L. Bonardet, J.B. d'Espinose, N. Melosh, J. Fraissard, Direct synthesis of AlSBA mesoporous molecular sieves: characterization and catalytic activities, Chem. Commun. 19 (1999) 1967–1968.

[36] Y.H. Yue, A. Gedeon, J.L. Bonardet, J.B. d'Espinose, N. Melosh, J. Fraissard, Direct incorporation of A1 in SBA mesoporous materials: characterization, stability and catalytic activity, Stud. Surf. Sci. Catal. 129 (2000) 209–218.

[37] H.M. Kao, C.C. Ting, S.W. Chao, Post-synthesis alumination of mesoporous silica SBA-15 with high framework aluminum content using ammonium hexafluoroaluminate, J. Mol. Catal. A: Chem. 235 (2005) 200–208.

[38] M.A.A. Aziz, N.H.N. Kamarudin, H.D. Setiabudi, H. Hamdan, A.A. Jalil, S. Triwahyono, Negative effect of Ni on PtHY in *n*-pentane isomerization evidenced by IR and ESR studies, J. Nat. Gas Chem. 21 (2012) 29–36.

[39] J.A. Lercher, A. Jentys, in: J. Cejka, H. van Bekkum, A. Corma, F. Schuth (Eds.), Introduction to Zeolite Science and Practice, third ed., Elsevier, Amsterdam, 2007, p. 452.

[40] C.A. Emeis, Determination of integrated molar extinction coefficients for infrared absorption bands of pyridine adsorbed on solid acid catalysts, J. Catal. 141 (1993) 347–354.

[41] N.H.N. Kamarudin, A.A. Jalil, S. Triwahyono, R.R. Mukti, M.A.A. Aziz, H.D. Setiabudi, M.N.M. Muhid, H. Hamdan, Interaction of Zn^{2+} with extraframework aluminum in HBEA zeolite and its role in enhancing *n*-pentane isomerization, Appl. Catal. A 431–432 (2012) 104–112.

[42] J.S. Beck, J.C. Vartuli, W.J. Roth, M.E. Leonowicz, C.T. Kresge, K.D. Schmitt, C.T-W. Chu, D.H. Olson, E.W. Sheppard, S.B. McCullen, J.B. Higgins, J.L. Schlenker, A new family of mesoporous molecular sieves prepared with liquid crystal templates, J. Am. Chem. Soc. 114 (1992) 10834–10843.

[43] R. Mokaya, W. Jones, Z. Luan, M.D. Alba, J. Klinowski, Acidity and catalytic activity of the mesoporous aluminosilicate molecular sieve MCM-41, Catal. Lett. 37 (1996) 113–120.

[44] Y. Jin, Y. Li, H. Wang, S. Zhao, Z. Lv, X. Du, Y. Sun, Textural mesoporosity and opening frame network of mesoporous MOR zeolites synthesized under intensifying perturbation conditions, Micropor. Mesopor. Mater. 153 (2012) 144–154.

[45] D. Trong On, S.M.J. Zaidi, S. Kaliaguine, Stability of mesoporous aluminosilicate MCM-41 under vapor treatment, acidic and basic conditions, Micropor. Mesopor. Mater. 22 (1998) 211–224.

[46] S. Shylesh, A.P. Singh, Heterogenized vanadyl cations over modified silica surfaces: a comprehensive understanding toward the structural property and catalytic activity difference over mesoporous and amorphous silica supports, J. Catal. 244 (2006) 52–64.

[47] J. Klinowski, Solid-state NMR studies of zeolite catalysts, Colloids Surf. 36 (1989) 133–154.

[48] W. Hu, Q. Luo, Y. Su, L. Chen, Y. Yue, C. Ye, F. Deng, Acid sites in mesoporous Al-SBA-15 material as revealed by solid-state NMR spectroscopy, Micropor. Mesopor. Mater. 92 (2006) 22–30.

[49] M. Bevilacqua, T. Montanari, E. Finocchio, G. Busca, Are the active sites of protonic zeolites generated by the cavities?, Catal Today 116 (2006) 132–142.

[50] S. Triwahyono, Z. Abdullah, A.A. Jalil, The effect of sulfate ion on the isomerization of *n*-butane to *iso*-butane, J. Nat. Gas Chem. 15 (2006) 247–252.

[51] S. Li, A. Zheng, Y. Su, H. Zhang, L. Chen, J. Yang, C. Ye, F. Deng, Brønsted/Lewis acid synergy in dealuminated HY zeolite: a combined solid-state NMR and theoretical calculation study, J. Am. Chem. Soc. 129 (2007) 11161–11171.

[52] M.C. Chao, H.P. Lin, C.Y. Mou, B.W. Cheng, C.F. Cheng, Synthesis of nano-sized mesoporous silicas with metal incorporation, Catal. Today 97 (2004) 81–87.

[53] S.M. Bradley, R.A. Kydd, Ga_{13}, Al_{13}, $GaAl_{12}$, and chromium-pillared montmorillonites: acidity and reactivity for cumene conversion, J. Catal. 141 (1993) 239–249.

[54] F. Patrick, S. Sugunan, Cracking of cumene on tungsten promoted ceria catalysts, React. Kinet. Mech. Catal. 103 (2011) 125–131.

[55] T. Mishra, K. Parida, Transition metal oxide pillared clay: 5. Synthesis, characterisation and catalytic activity of iron ± chromium mixed oxide pillared montmorillonite, Appl. Catal. A: Gen. 174 (1998) 91–98.

[56] A. Gil, L.M. Gandia, M.A. Vicente, Recent advances in the synthesis and catalytic applications of pillared clays, Catal. Rev. Sci. Eng. 42 (2000) 145–212.

[57] A. Corma, B.W. Wojciechowski, The catalytic cracking of cumene, Catal. Rev. Sci. Eng. 24 (1982) 1–65.

[58] N.N. Ruslan, N.A. Fadzlillah, A.H. Karim, A.A. Jalil, S. Triwahyono, IR study of active sites for *n*-heptane isomerization over MoO_3–ZrO_2, Appl. Catal. A 406 (2011) 102–112.

[59] R.M. Koros, E.J. Nowak, A diagnostic test of the kinetic regime in a packed bed reactor, Chem. Eng. Sci. 22 (1967) 470.

[60] A. de Lucas, P. Canizares, A. Duran, A. Carrero, Coke formation, location, nature and regeneration on dealuminated HZSM-5 type zeolites, Appl. Catal. A 156 (1997) 299–317.